This article has been accepted for inclusion in a future issue of this journal. Content is final as presented, with the exception of pagination.

Epitaxial Aluminum Scandium Nitride Super High Frequency Acoustic Resonators

Mingyo Park, *Senior Member, IEEE*, Zhijian Hao, *Senior Member, IEEE*, Rytis Dargis, Andrew Clark, and Azadeh Ansari, *Member, IEEE*

***Abstract*— This paper demonstrates super high frequency (SHF) Lamb and surface acoustic wave resonators based on single-crystal orientation Aluminum Scandium Nitride (AlScN) thin films grown on silicon substrates by molecular beam epitaxy (MBE). We report on the experimental frequency response and electromechanical properties of 400 nm-thick crystalline AlScN acoustic resonators with up to 12% Sc/(Sc+Al) ratio. The film thickness is optimized for operation at the SHF range, targeting emerging wireless communication standards, such as 4G LTE/5G. We report on high-performance acoustic devices that take advantage of the crystallinity, and high piezoelectric properties of 400 nm-thick epitaxial AlScN films. Our work presents enhanced effective electromechanical coupling coefficients (k_{eff}^2) up to 5.3% and unloaded quality factors (Q_m) of ∼192 at 3-10 GHz. However, fabrication challenges due to the high-stress levels of sub-micron AlScN epi-layers grown on Si substrates remain challenging and will be discussed in this paper. [2019-0231]**

***Index Terms*— Acoustic resonators/filters, surface acoustic wave resonators, lamb wave resonators, epitaxial aluminum nitride, scandium, molecular beam epitaxy (MBE).**

I. Introduction

THE next generation of wireless standards (*e.g.* "5G") is regarded as a promising solution with satisfying demands for the drastically increasing number of bands and the complexity in the wireless communication system. Emerging 5G, Wi-Fi and 4G LTE communication standards call for high-performance acoustic Micro-Electro-Mechanical (MEMS) filters. Such acoustic filters are highly desirable for operation at new RF band sections, starting from the frequency range of LTE bands at 3.4-3.8 GHz [1], [2], up to millimeter-wave 5G bands at 26 GHz [1], [3]. High-performance acoustic resonators and filters, such as surface acoustic wave (SAW) [4] and bulk acoustic wave (BAW) [5] resonators are realized in different piezoelectric material systems. Amongst them, aluminum nitride (AlN) has been popular mainly due to CMOS compatibility and well-developed micromachining techniques.

The key parameters that define the figures of merit of an acoustic filter include 1) quality factor (Q), which determines the insertion loss of the filter and steep skirts selectivity, and 2) electromechanical coupling coefficient (k^2), which determines the filter bandwidth, and 3) thermal conductivity, which affects the power handling and device self-heating. It has been reported that there is a strong correlation between the crystallinity of the piezoelectric device layer and 1) Q-factor [6], 2) piezoelectric coefficients that affect k^2 of the device [7], and the 3) thermal conductivity of the material [8].

Limited Q-factors have been observed in polycrystalline AlN films due to an increase in the scattering losses at the grain boundaries of films with large Full Width at Half Maximum (FWHM) values [6]. Furthermore, limited k^2 values have been caused by the low FWHM values, and poor crystal quality of thin films, affecting the bandwidth of the filter [7].

Additionally, recent work [8] on the dependency of AlN thermal conductivity and the crystal quality has illustrated that the thermal conductivity of AlN is strongly reduced in sub-micron poly-crystalline thin-films due to phonon boundary scattering caused by Al vacancies.

The three aforementioned parameters justify the investigation of epitaxial nitride piezoelectric materials for acoustic devices, particularly targeting <1 μm thick films.

In addition to improving the crystallinity of piezoelectric layers, introducing scandium (Sc) to AlN sputtered films has shown enhanced piezoelectricity, to compensate for the moderate k^2 of pure AlN resonators. This has led to an increase in the piezoelectric coefficients of $Sc_{0.4}Al_{0.6}N$, up to 4 - 5 times larger than pure AlN [9]. Various growth methods and conditions to deposit AlN/AlScN have been reported to date [10], [11]. Reactive magnetron sputtering is the most common method for the deposition of AlN and AlScN owing to low cost and relatively high deposition rate [11]. Although the crystal quality of the sputtered layers is inferior to those grown using epitaxial methods with high vacuum conditions, the effect of poly crystallinity can be averaged out for thickness > 1 μm thick films [12]–[14], and has been

Manuscript received October 11, 2019; revised June 3, 2020; accepted June 5, 2020. This work was supported in part by the National Science Foundation under Grant Eccs-1542174, in part by the IQE PLC, in part by the Institute for Electronics and Nanotechnology (IEN) Cleanroom Facility at the Georgia Institute of Technology (Devices Were Fabricated), and in part by the National Nanotechnology Coordinated Infrastructure (NNCI) through the National Science Foundation under Grant ECCS-1542174. Subject Editor R. N. Candler. *(Corresponding author: Mingyo Park.)*

Mingyo Park, Zhijian Hao, and Azadeh Ansari are with the School of Electrical and Computer Engineering, Georgia Institute of Technology, Atlanta, GA 30308 USA (e-mail: m.park@gatech.edu).

Rytis Dargis and Andrew Clark are with IQE plc, Greensboro, NC 27409 USA (e-mail: RDargis@iqep.com).

Color versions of one or more of the figures in this article are available online at http://ieeexplore.ieee.org.

Digital Object Identifier 10.1109/JMEMS.2020.3001233

1057-7157 © 2020 IEEE. Personal use is permitted, but republication/redistribution requires IEEE permission. See https://www.ieee.org/publications/rights/index.html for more information.

Authorized licensed use limited to: Georgia Institute of Technology. Downloaded on July 09,2020 at 05:52:30 UTC from IEEE Xplore. Restrictions apply.

This article has been accepted for inclusion in a future issue of this journal. Content is final as presented, with the exception of pagination.

the conventional method for commercially-available acoustic filters [15], [16]. However, the crystal properties of sputtered AlN films degrade with thinning down the film thickness, particularly below 500 nm, and ultimately limits the acoustic device performance for >2.6 GHz frequency range [17]. Recent work has reported on using optimized seed layers to deposit sputtered AlN thin films [18]; however, epitaxial growth can inherently yield higher crystal qualities, lower FWHM values, and higher thermal conductivities for <500 nm thick films.

A common epitaxial growth method of AlN is metal-organic chemical vapor deposition (MOCVD), which is widely used for the growth of III-N layers for electronic and photonic devices. Although this technique provides high-quality crystallinity [19], it has been challenging for the growth of AlScN thin films because of the absence of scandium precursors and the required phase separation for the reliable decomposition of the precursors at typical MOCVD process temperatures, so far [11]. There has only been one report of successful MOCVD growth of AlScN films, recently demonstrated in [20].

Another method for the epitaxial growth of AlScN films is MBE. Ref [21] reported on the epitaxial growth of AlScN films by MBE for high-power device applications. Our group has been the first to show acoustic devices based on MBE-grown AlScN films [22]–[25]. In this work, we extensively characterize SAW and LWR resonators based on 400 nm-thick AlN and AlScN epi-layers grown on Si substrates by MBE, which is based on the reaction of the atomic or molecular beam with a heated crystalline surface in an ultra-high vacuum condition [26].

By taking advantage of the high-quality ultra-thin (400 nm-thick) epitaxial piezo-layers, this work enables high-performance acoustic resonators with the 3-10 GHz operating frequency range. Despite the enhanced film quality, the main problem with the epitaxial growth of AlScN films is controlling the stress in this ternary alloy that complicates the fabrication process, particularly for the final release step of suspended structures, discussed in detail in Section IV-B.

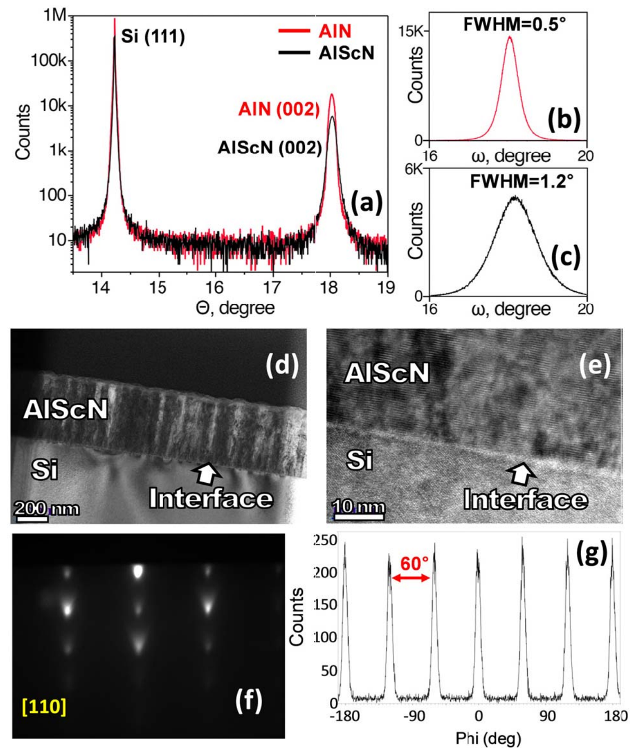

Fig. 1. 400 nm-thick AlScN and AlN film characterization: (a) X-ray diffraction (XRD) characterization, (b) omega (ω) scan of AlN, and (c) omega (ω) scan of AlScN thin films grown directly on Si (111). (d) Scanning electron microscope (SEM) image of the cross section of AlScN (0002) layer, (e) high-resolution transmission electron microscopy (HRTEM) of AlScN (0002) layer on Si (111) in <110> azimuth. (f) High-energy electron diffraction (RHEED) pattern of AlScN on Si (111) in <110> azimuth. (g) The XRD (103) phi scan of AlScN on Si films.

II. Material Characterization

A. AlScN Films Grown by MBE

Epitaxial AlN and AlScN thin films with 400 nm thickness were grown on 4-inch Si (111) wafers in a ultra high vacuum (UHV) environment. Al and Sc were evaporated from effusion cells and activated nitrogen was introduced from a plasma source [26]. Metal fluxes from the effusion cells were adjusted to get 12% Sc concentration in the AlScN layer. The crystal structure of the AlN and AlScN grown on Si (111) was analyzed using X-ray diffraction (XRD) [22]–[24], [27]. Fig.1(a) illustrates XRD $2\theta/\omega$ scans of the AlN/AlScN films on Si including only diffraction maxima attributed to Si <111> and AlN/AlScN <0001>, indicating that both piezoelectric nitride layers have a single out-of-plane crystallographic orientation. Fig.1(b)-(c) illustrate the XRD ω scan of the AlN/AlScN (0002) layers, demonstrating FWHM values of (0002) peaks of 0.5°/1.2° for AlN/$Al_{0.88}Sc_{0.12}N$ layers. Generally, the wider RC (0002) peak of AlScN compared to AlN is expected due to local lattice distortion by incorporation of scandium atoms in the wurtzite AlN crystal lattice [28]. However, these values are lower compared to that of sputter-deposited AlN and AlScN films [29], [30], more prominent at submicron thicknesses, which indicates the higher crystal quality of the epitaxially-grown materials [21]. As shown in Fig. 1(d), AlScN has a columnar structure with the columns rotated around the c-axis, as can be seen from cross-section transmission electron images taken in <110> azimuth of the Si substrate. This is typical for III-N and Sc-III-N layers grown on sapphire [31]. The layer has single-out-of-plane crystal orientation from the interface without any transitional layer, as seen in the HRTEM image presented in Fig. 1(e). Additionally, in-situ reflecting high energy electron diffraction (RHEED) patterns in <110> azimuth confirmed that the nitride layers have single out-of-plane orientation, as shown Fig.1(f). The in-situ RHEED analysis shows characteristic six-fold in-plane rotation symmetry of the crystal structure. This was also confirmed by the XRD phi-scan of (103) asymmetric peak of the AlScN layers as described in Fig.1(g), showing that the columns are rotated by 60° from each other. Sc/(Sc+Al) of 12% was confirmed by Rutherford backscattering spectrometry (RBS) analysis. Higher Sc concentration is desired for the stronger

Authorized licensed use limited to: Georgia Institute of Technology. Downloaded on July 09,2020 at 05:52:30 UTC from IEEE Xplore. Restrictions apply.

This article has been accepted for inclusion in a future issue of this journal. Content is final as presented, with the exception of pagination.

piezoelectric response but renders the growth challenging and is expected to further increase the FWHM values [32].

B. Material Characterization of AlScN Films

In this section, the 1) piezoelectric coefficients, 2) elastic properties, and 3) dielectric constants of AlScN films are theoretically analyzed based on the Sc/(Al+Sc) ratio. Such material constants define the phase velocity (Sec. II-C) and electromechanical properties (Sec. III-A) of AlScN devices.

The evaluated piezoelectric coefficient and elastic constants of $Al_{1-x}Sc_xN$ are calculated by the flowing equations below, where x is Sc/(Al+Sc) ratio [33]:

$$\begin{aligned} e_{15} &= -0.367\,(1-x) - 0.435x + 0.417x\,(1-x)\,, \\ e_{31} &= -0.424\,(1-x) - 0.286x - 0.615x\,(1-x)\,, \\ e_{33} &= 1.449\,(1-x) + 8.182x - 5.912x\,(1-x)\,. \end{aligned} \quad (1)$$

$$\begin{aligned} C_{11}\,(x) &= 378.8\,(1-x) + 263.9x - 210.3x(1-x), \\ C_{12}\,(x) &= 128.9\,(1-x) + 185.1x - 61.9x\,(1-x)\,, \\ C_{13}\,(x) &= 96.1\,(1-x) + 121.5x + 78.9x\,(1-x)\,, \\ C_{33}\,(x) &= 357.5\,(1-x) - 51.3x - 101.4x\,(1-x)\,, \\ C_{44}\,(x) &= 112.4\,(1-x) + 159.0x - 137.3x\,(1-x)\,. \end{aligned} \quad (2)$$

A full set of piezoelectric coefficients, e_{ij} (Cm^{-2}), and composition-dependent elastic constants C_{ij}(GPa) are shown in (1) and (2), which are derived from density functional theory (DFT) calculations using large periodic supercells and the Berry-phase theory of polarization [33].

It has been reported that the relative dielectric constant of the films shows an increasing tendency as Sc concentration is increased [34]. The relative dielectric constant of $Al_{1-x}Sc_xN$ can be evaluated by the flowing equations below [35]:

$$\begin{aligned} \varepsilon_{33,f} &= (9.0 \pm 0.6) + (20.9 \pm 0.6)\,x + (47.5 \pm 20.1)\,x^2, \\ \varepsilon_{33} &= \varepsilon_{33,f} - \frac{e_{33}^2}{\varepsilon_0 C_{33}}. \end{aligned} \quad (3)$$

where $\varepsilon_{33,f}$ is the relative dielectric coefficient (clamped), ε_0 is the vacuum permittivity, e_{33} is the piezoelectric coefficient, and C_{33} is the elastic stiffness at the constant electric field. On the other hand, it has been found that the dielectric constant of AlN at high frequency decreases to 4.84 compared to the dielectric constant used for AlN (9.1) at low frequencies [22]–[24], [36]. In this work, we utilized the dielectric constant for a high-frequency response along with the Sc concentration [36].

C. Phase Velocity Dependence on Sc/(Al+Sc) Ratio

The phase velocities of SAW and Lamb-wave (LW) modes depend on the longitudinal (P-wave) wave and shear wave (S-wave). The P-wave (υ_p) and S-wave (υ_s) propagating along the <100> direction are defined by the following equation [12]:

$$\begin{aligned} \upsilon_p &= \sqrt{C_{11}/\rho}, \\ \upsilon_s &= \sqrt{C_{44}/\rho}. \end{aligned} \quad (4)$$

where C_{11} and C_{44} are elastic coefficients, determined by the wave propagation and polarization directions. ρ denotes material density. Besides the reduction of the elastic coefficients (Eq. 2), the mass density of $Al_{1-x}Sc_xN$ films slightly increases as the Sc concentration increases, [35], further decreasing the AlScN film phase velocity. Fig. 2(a) shows the phase velocity of the AlN and $Al_{0.88}Sc_{0.12}N$ vs. the normalized thickness (h/λ) using different pitch sizes of the SAW devices. Fig. 2(b) illustrates the resonant peak frequency shift observed in the same LWR design with a pitch of 300 nm, based on AlN and $Al_{0.88}Sc_{0.12}N$ films. The resonant peak shift of $Al_{0.88}Sc_{0.12}N$ compared to pure AlN is due to the reduced phase velocity [37].

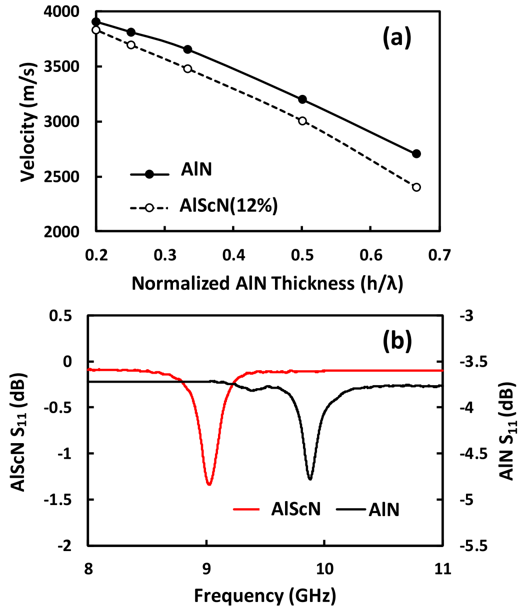

Fig. 2. (a) Dispersion curve of SAW phase velocity measured for AlN and $Al_{0.88}Sc_{0.12}N$ on Si substrate, and (b) resonant peak frequency shift of the same LWR design for AlN and $Al_{0.88}Sc_{0.12}N$, showing the spring softening effect in $Al_{0.88}Sc_{0.12}N$ resonators.

III. Resonator Electromechanical Characterization

Higher piezoelectric coupling coefficient (K^2) is obtained in resonators that use AlScN compared to AlN resonators due to higher piezoelectric coefficients [7], [9], [38]. The piezoelectric response can be boosted by 4-5 times with an increased Sc concentration up to ~40% [9]. Besides the known effect of Sc concentration, the crystal quality of the piezoelectric material plays an important role in defining the piezoelectric response and ultimately, the performance of the acoustic filters [17]. The dependence of the acoustic resonator/ filter figure of merit (K^2) for SAW and Lamb-wave resonator (LWR), on the piezoelectric coefficients ($e_{33,31}$) is presented in equation (5): [29], [39]–[41]

$$K^2 = \frac{e_{33,31}^2}{c \cdot \varepsilon_o \varepsilon_r}. \quad (5)$$

where c is the effective elastic constant, e_{33}/$-e_{31}$ is the longitudinal/transversal piezoelectric coefficient, ε_o is vacuum permittivity and ε_r is the relative dielectric constant.

Authorized licensed use limited to: Georgia Institute of Technology. Downloaded on July 09,2020 at 05:52:30 UTC from IEEE Xplore. Restrictions apply.

This article has been accepted for inclusion in a future issue of this journal. Content is final as presented, with the exception of pagination.

TABLE I
MATERIAL CONSTANTS USED IN FINITE ELEMENT SIMULATIONS

	Symbol	AlN	$Al_{0.88}Sc_{0.12}N$	Units
Stiffness constants	C_{11}	379	343	$10^9 N/m^2$
	C_{12}	129	129	
	C_{13}	96	107	
	C_{33}	357	298	
	C_{44}	112	103	
	C_{66}	110	110	
Piezoelectric constants	e_{15}	-0.367	-0.331	C/m^2
	e_{31}	-0.424	-0.472	
	e_{33}	1.449	1.632	
Dielectric constants	ε	4.84*	5.13*	
		9	11.16	
Density	ρ	3300	3333	kg/m^3

*High frequency dielectric constants

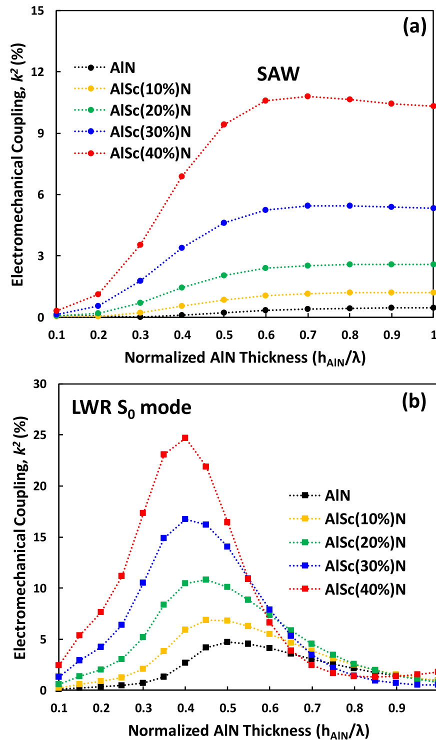

Fig. 3. FEA simulation results of the electromechanical coupling coefficient (k^2) of (a) SAW and (b) LWR fundamental symmetric mode (S_0) vs. the normalized thickness ($\frac{h_{AlN}}{\lambda}$). A 400 nm-thick $Al_{1-x}Sc_xN$ piezo-layer is used with 80 nm of Ti/Au top electrode, at various x=Sc/(Al+Sc) ratios.

The electromechanical coupling of the $Al_{1-x}Sc_xN$ resonators is simulated using COMSOL finite element analysis (FEA) using Eq. sets (2) and (3), with varying x, as shown in Table I. Fig. 3. demonstrates the FEA simulated electromechanical coupling coefficient (k^2) of SAW and LWRs [12], [42], based on the normalized AlN/AlScN thickness using: [40], [42]

$$k^2 = \frac{v_0^2 - v_m^2}{v_0^2} = 2 \times \frac{v_0 - v_m}{v_0}. \tag{6}$$

The k^2 is evaluated based on the phase velocity of electrically free AlN surface (v_o) and the phase velocity of the shorted surface (v_m) using Eq. (6). The dispersion curve is characterized by using the lowest order of symmetric LW mode (S_0) with

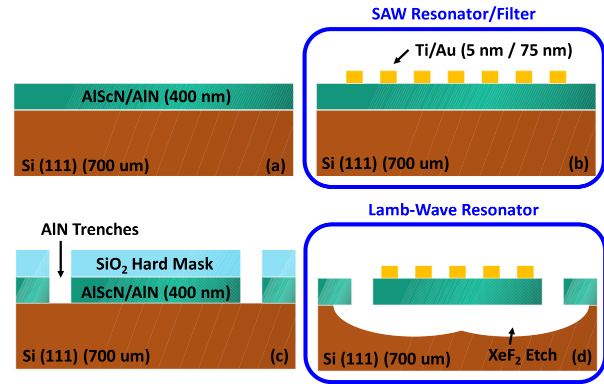

Fig. 4. (a) 400 nm AlN-on-Si starting epi-wafer. (b) The fabrication process of a one-step exposure of the SAW devices. (c) Patterning Oxide hard mask and etching AlN in a Cl_2-based plasma etching. (d) Isotropic etching of the Si substrate to release the LWR membrane [23], [24].

electrodes thickness of 80 nm of Ti/Au. The k^2 is extracted based on the Sc concentration ranging from 0 to 40%.

The k^2 of S_0 mode increases as Sc concentration increases and can reach values up to 25 % when a 40% Sc/(Sc+Al) ratio is reached, confirming the applicability of AlScN films with high Sc dopings for 5G applications. As shown in Fig. 3 (b), the normalized thickness of 0.5 provides the highest k^2 of 4.7%/ 7.56% for AlN/$Al_{0.88}Sc_{0.12}N$ based-devices, showing the 1.6 times increased k^2 value for the $Al_{0.88}Sc_{0.12}N$ compared to pure AlN device. While higher Sc concentrations are desirable for higher k^2 values, the high levels of stress and cracks in the thin films limited us from further increasing the Sc/(Sc+Al) ratio in this work.

IV. FABRICATION PROCESS

A. SAW and Lamb-Wave Resonators

The fabrication steps are summarized in Fig. 4 by illustrating the cross-section of the devices. Fig. 4(a)–(b) depict the fabrication of a SAW resonator/filter and Fig. 4(c)–(d) show the fabrication process of a LWR. Each interdigitated transducer finger width is 200 nm and is defined with electron-beam lithography (EBL) and Ti/Au with a thickness of 5 nm/75 nm is deposited as the top inter-digitated (IDT) electrode.

The fabrication of SAW resonators/filters is a simple one-mask process, without the need to suspend the piezo-layer. Fabrication of LW devices requires plasma etching of AlN/AlScN trenches using an oxide hard mask. After etching 400 nm-thick AlN/AlScN layers, the device is exposed to xenon difluoride (XeF_2) gas for the final release step to create suspended structures from the host Si substrate. Fig. 5 shows the SEM images of the SAW and LW resonators.

B. AlScN Resonator Fabrication Challenges

Etching high crystal quality AlScN films and the subsequent release of the device is challenging due to 1) low etch rate and poor selectivity of epi AlScN to photoresist or SiO_2 mask layer, and 2) deformation of the device due to stress. To pattern the trenches, AlN/AlScN layers are etched by Cl_3-based thermal inductively coupled plasma (ICP). It has been reported that the etch rate of AlScN films drops by

Authorized licensed use limited to: Georgia Institute of Technology. Downloaded on July 09,2020 at 05:52:30 UTC from IEEE Xplore. Restrictions apply.

This article has been accepted for inclusion in a future issue of this journal. Content is final as presented, with the exception of pagination.

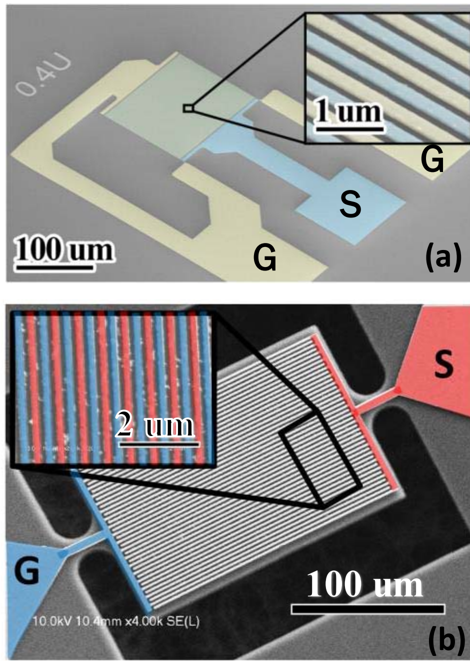

Fig. 5. SEM images of the fabricated devices of (a) SAW with 400 nm of pitch width and (b) LWR with 400 nm of pitch size [22], [24].

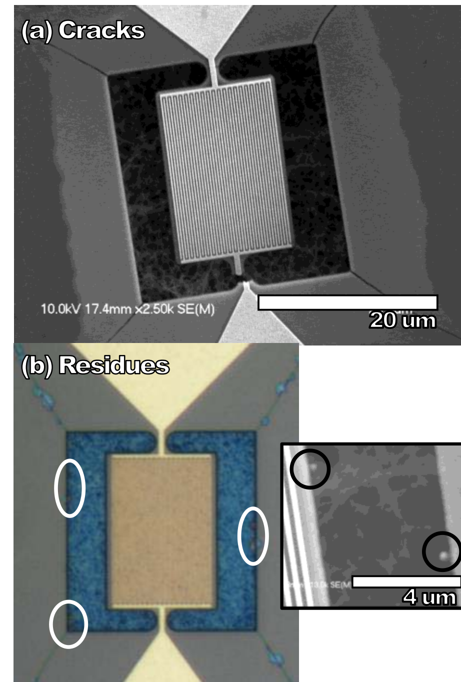

Fig. 6. (a) SEM and (b) microscope/SEM images of AlScN resonators, showing (a) film cracks due to the film stress on the tethers and the outer frame and (b) residues due to re-deposition on the outer frame of the trenches.

∼25% compared to pure AlN films [21], [43]. Compared to AlN, the etching of AlScN films shows low etch rates and poor selectivity to the mask layer because AlScN films are more resistant to BCl_3-based recipes [44]. Moreover, re-deposition effects occur owing to maintained and accumulated Sc-based non-volatile byproducts during the etching process [21], [44].

Besides the effect of Sc concentration on the etch rate, the etch rate is also strongly dependent on the crystalline quality of the AlN films [45]. AlN films with poorer crystallinity are more susceptible to be attacked by etchant due to the greater number of weakened bonds [46]. Thus, single-crystal orientation AlN films show significantly lower etch rates compared to polycrystalline AlN grown by sputter deposition techniques.

Furthermore, the film cracks are caused by thin-film stress during the release step. Fig. 6 illustrates SEM and microscope images of AlN/AlScN LW devices. The stress gradient applied to a sub-micron thickness of AlN/AlScN is strong enough to break two tethers and make cracks on the edge of the device as shown in Fig. 6(a). Flakes appear because of the re-deposition of Sc-based non-volatile byproducts from the AlScN etching process shown in the outer frame of the AlN trenches in Fig. 6(b). Considering such challenges, the future work would focus on the mitigation of re-deposition and precise control of the thin film stress to improve the quality of the ultra-thin epitaxial AlScN resonators and their yield.

V. Device Characteristics and Experimental Results

A. Frequency Response and Resonant Mode Characteristic of SAW and Lamb-Wave Resonators

The devices are measured using the Keysight N54244B PNA microwave network analyzer. Fig. 7(a)–(b) show

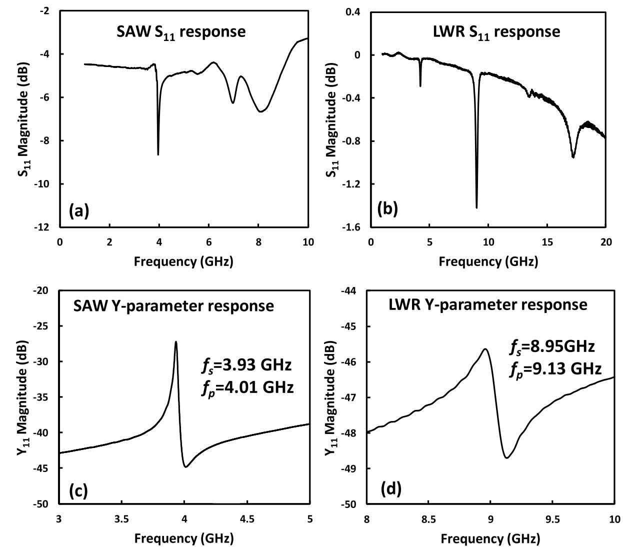

Fig. 7. Measurement results of AlScN/Si SAW and AlScN LW resonators. (a)-(b): Wideband frequency response of SAW with frequency range at 1-10 GHz and LW with frequency range at 1-20 GHz. (c)-(d): Zoomed-in admittance plots of SAW and LW resonators [22], [23].

wide band scattering matrix (S)-parameters tested over the frequency range from 1 to 10 GHz for 400 nm pitch size of $Al_{0.88}Sc_{0.12}N$ SAW devices and 1-20 GHz for 300 nm pitch size of the $Al_{0.88}Sc_{0.12}N$ LW devices. Fig. 7(c)–(d) demonstrates corresponding zoomed-in peaks of each resonator in Y-parameter. In the wideband frequency response, LWR shows a multi-resonant frequency response showing various asymmetric (A_i) and symmetric (S_i) modes [42], [47], [48].

Authorized licensed use limited to: Georgia Institute of Technology. Downloaded on July 09,2020 at 05:52:30 UTC from IEEE Xplore. Restrictions apply.

This article has been accepted for inclusion in a future issue of this journal. Content is final as presented, with the exception of pagination.

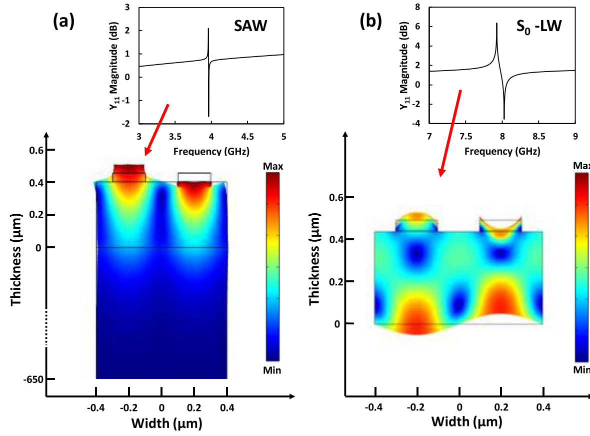

Fig. 8. Simulation results of the resonance displacement mode shapes: (a) SAW and (b) fundamental Symmetric (S_0) LW mode, showing structural deformation at the resonant frequency of 3.97 and 7.9 GHz, with thickness of 400 nm AlN piezoelectric layer and 80 nm Ti/Au electrode.

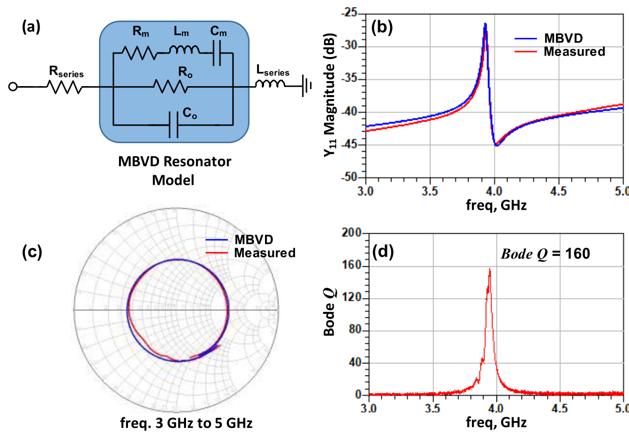

Fig. 9. Frequency characterization of SAW resonator with (a) Modified Butterworth-Van Dyke (MBVD) model. The measured and MBVD fitted Zoomed-in Y_{11} magnitude response of (b) SAW with 400 nm pitch is plotted at the resonant frequency of 3.9 GHz. Extracted Bode Q of SAW based on S_{11} with transforming the source impedance to 57.96+j18.5Ω: (c) the measured and MBVD fitted result plotted on the Smith chart and (d) the evaluated Bode Q of 160.

Fig. 8 illustrates the FEA simulation result of the excited two resonance modes along with the displacement mode shape at the resonance frequency of 3.9 and 7.9 GHz. Fig. 8(a) shows the mode shape of the SAW device on Si substrate. Fig. 8(b) describes the S_0 mode of LWR, showing the symmetric deformation shape in the piezoelectric layer. The calculated phase velocity of SAW / LWR with the 400 nm pitch is 3104 / 6376 m/s, which is matched with the measurement results.

B. Motional Parameter Characterization

The measured frequency responses of SAW resonators are fitted with the Modified Butterworth-Van Dyke (MBVD) model, with center frequency at 3.97 GHz, as shown in Fig. 9. In the MBVD model, the static capacitor (C_o) and resistor (R_o) are contained as the dielectric loss in the substrate, and the motional branch consists of the motional resistor (R_m), inductor (L_m), and capacitor (C_m). The C_o and R_o are evaluated

TABLE II

ELECTROMECHANICAL CHARACTERISTICS EXTRACTED FROM MBVD MODEL FITTING OF AlScN RESONATORS

	f_{res} (GHz)	C_o (fF)	C_m (fF)	L_m (nH)	R_m (Ω)	Q_m
#,a SAW	3.93	290	*10.7*	*152.8*	*19.6*	*192*

#: $Al_{0.82}Sc_{0.18}N$ film, a: 400 nm pitch 1-port with reflector

by exploiting imaginary and real parts of the off-resonance of *Y-/Z-* parameters [42], [49], and Sonnet electromagnetic (EM) simulation. The evaluated C_o is 290 fF for SAW resonators. The unloaded quality factor (Q_m) of the resonator is estimated by using the motional branch [49]. The extracted Q_m of SAW resonator with a value of 192.

Another method to evaluate Q is using Bode Q based on S_{11}. The Bode Q is computed using the motional branch of the S_{11} fitted MBVD curves following by [37]:

$$Q_{bode} = \omega \times \frac{|S_{11}|\, group_delay(S_{11})}{1 - |S_{11}|^2}. \quad (7)$$

The Q_{bode} is defined by using the phase group delay of S-parameter. Fig.9(c) illustrates the S_{11} response of the measured and MBVD fitted model on the Smith chart. The continuous Q circle is placed in the center of the smith chart using source impedance matching [50]. Fig.6 shows the evaluated unloaded Q along with the frequency response achieving Q_{bode} of 160. Table II summarizes the MBVD parameters and Q_m of the SAW device.

SAW reflectors are fabricated in the same fabrication step, whereas the trenches for LWR are fabricated in a separate step and thus prone to lithography alignment error. A waveguide with rough sidewalls caused by etching AlN/AlScN trenches lowers Q [44]. Moreover, utilizing epitaxial metal electrodes, instead of sputtered metal electrodes is necessary to maximize the Q of acoustic devices. This reduces the scattering losses of polycrystalline metal layers and the poor-quality metal-piezoelectric interface [51]. The Q factors reported in this work would improve from using an all-epitaxial resonant stack. Furthermore, better anchor designs, use of phononic crystals, and improvement of the fabrication process could enhance acoustic wave confinement in the resonator structure and thus enhance anchor Q of the LWR designs [23], [52].

Next, we characterize the effective electromechanical coupling coefficient (k^2_{eff}) of the SAW and LWRs [22], [23], using:

$$k^2_{eff} = \frac{\pi^2}{4} \times \frac{f_s(f_p - f_s)}{f_p^2}. \quad (8)$$

where f_s is the series and f_p is the parallel resonant frequency which is determined from measured admittance (Y_{11})-parameter of the device. Table III summarizes the evaluated k^2_{eff} of SAW and LWR devices in $Al_{1-x}Sc_xN$ films.

C. The Dependency of Resonance Frequency on Temperature

In order to study the temperature characteristic of the resonance frequency of SAW and LW resonators, temperature measurements in the range of 150 to 600 K were performed

Authorized licensed use limited to: Georgia Institute of Technology. Downloaded on July 09,2020 at 05:52:30 UTC from IEEE Xplore. Restrictions apply.

This article has been accepted for inclusion in a future issue of this journal. Content is final as presented, with the exception of pagination.

TABLE III
EXPERIMENTALLY EVALUATED ELECTROMECHANICAL PARAMETERS OF EPITAXIALLY-GROWN AlN AND AlScN RESONATORS

	Sc/(Sc+Al) (%)	Pitch (um)	f_s (GHz)	f_p (GHz)	k_{eff}^2 (%)
SAW-MBE AlScN/Si	23	0.4	3.93	4.01	4.9
SAW-MBE AlScN/Si[20]	12	0.4	3.626	3.682	3.7
LWR-MBE AlN/Si[23]	0	0.3	9.823	9.991	4.1
LWR-MBE AlN/Si[23]	0	0.4	7.932	8.811	5.33
LWR-MBE AlScN/Si[23]	12	0.3	8.951	9.132	4.8

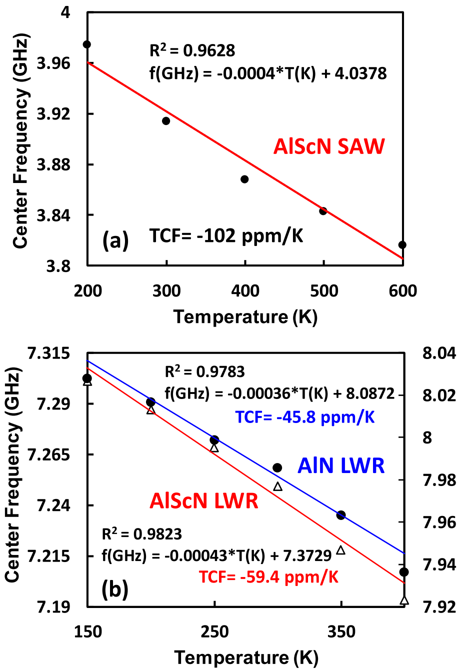

Fig. 10. The measurement result of temperature characteristics of acoustic MEMS resonators with temperature range from 200-600 K for (a) AlScN SAW resonator and 150-400 K for (b) AlN/AlScN LWRs.

using a cryostat probe station ARS 17-A269. Fig. 10 shows the temperature coefficient of frequency (TCF) measurement results of SAW and LW resonators, showing the resonance frequency variation as a function of temperature. The measured TCF ($=\Delta f/f.\ \Delta T$) value of SAW is -102 ppm/K as shown in Fig. 10(a), and TCF value of LWR is $-45.8/-59.4$ ppm/k for AlN/AlScN as presented in Fig. 10(b). LWR has a lower TCF value than SAW devices due to a fully suspended geometry which can avoid stress based on a mismatch of the coefficient of thermal expansion between AlN and Si [53]. Furthermore, AlScN has a slightly higher TCF value, caused by increased thermal expansion and decreased elastic modulus due to the Sc composition in the AlN film [53]. It has been reported [54], [55] that AlN film has a smaller TCF value compared to other piezoelectric material counterparts, such as ZnO or $LiNbO_3$, and thus, AlN resonators are better candidates for frequency-stable acoustic devices for high-temperature operation.

VI. CONCLUSION

In this paper, 400nm-thick epitaxial AlN and $Al_{0.88}ScAl_{0.12}N$ films were investigated for the design of acoustic MEMS resonators, targeting the 3-10 GHz frequency range. We took advantage of the high crystal quality of ultra-thin AlN/AlScN epi-layers, as well as the enhanced electromechanical coupling coefficient by incorporation of Sc to AlN epitaxial films. The variance of phase velocity due to the softening effect from Sc composition in AlScN films was verified with experimental results. This is the first demonstration of acoustic devices fabricated using epitaxial AlScN films, showing significant improvement of k_{eff}^2 at the super-high frequency range as summarized in Table III.

ACKNOWLEDGMENT

The authors would like to acknowledge Mr. D. Kim's help with the E-beam lithography process.

REFERENCES

[1] J. B. Shealy *et al.*, "Low loss, 3.7 GHz wideband BAW filters, using high power single crystal AlN-on-SiC resonators," in *IEEE MTT-S Int. Microw. Symp. Dig.*, Honololu, Hi, USA, Jun. 2017, pp. 1476–1479.

[2] *LTE Frequency Bands, Spectrum & Channels*. Accessed: May 12, 2019. [Online]. Available: https://www.electronics-notes.com/articles/connectivity/4g-lte-long-term-evolution/frequency-bands-channels-spectrum.php

[3] *5G Spectrum Bands*. Accessed: Jan. 1, 2019. [Online]. Available: https://gsacom.com/5g-spectrum-bands/

[4] T. Takai *et al.*, "I.H.P. SAW technology and its application to microacoustic components (Invited)," in *Proc. IEEE Int. Ultrason. Symp.*, Washington, DC, USA, Sep. 2017, pp. 1–8.

[5] R. Ruby, "A snapshot in time: The future in filters for cell phones," *IEEE Microw. Mag.*, vol. 16, no. 7, pp. 46–59, Aug. 2015.

[6] L. Shu *et al.*, "The characterization of surface acoustic wave devices based on AlN-metal structures," *Sensors*, vol. 16, no. 4, p. 526, Apr. 2016.

[7] E. Yarar, V. Hrkac, C. Zamponi, A. Piorra, L. Kienle, and E. Quandt, "Low temperature aluminum nitride thin films for sensory applications," *AIP Adv.*, vol. 6, no. 7, Jul. 2016, Art. no. 075115.

[8] R. L. Xu *et al.*, "Thermal conductivity of crystalline AlN and the influence of atomic-scale defects," *J. Appl. Phys.*, vol. 126, no. 18, 2019, Art. no. 185105.

[9] K. Umeda, H. Kawai, A. Honda, M. Akiyama, T. Kato, and T. Fukura, "Piezoelectric properties of ScAlN thin films for piezo-MEMS devices," in *Proc. IEEE Int. Conf. Micro Electro Mech. Syst.*, Taipei, Taiwan, Mar. 2013, pp. 733–736.

[10] C.-M. Yang and S.-K. Kim, "AlN epitaxial film growth using MOCVD for a GHz-band FBAR," *J. Korean Phys. Soc.*, vol. 55, no. 1, pp. 1132–1135, Sep. 2009.

[11] P. O. Persson *et al.*, "Microstructure and dielectric properties of piezoelectric magnetron sputtered W-$Sc_xAl_{1-x}N$ thin films," *J. Appl. Phys.*, vol. 111, no. 9, May 2012, Art. no. 093527.

[12] J. Zou, C. M. Lin, C. S. Lam, and A. P. Pisano, "Transducer design for AlN Lamb wave resonators," *J. Appl. Phys.*, vol. 121, no. 15, Apr. 2017, Art. no. 154502.

[13] A. Konno *et al.*, "ScAlN Lamb wave resonator in GHz range released by XeF_2 etching," in *Proc. IEEE Int. Ultrason. Symp.*, Prague, Czech, Jul. 2013, pp. 1378–1381.

[14] L. Colombo, A. Kochhar, C. Xu, G. Piazza, S. Mishin, and Y. Oshmyansky, "Investigation of 20% scandium-doped aluminum nitride films for MEMS laterally vibrating resonators," in *Proc. IEEE Int. Ultrason. Symp.*, Washington, DC, USA, Sep. 2017, pp. 1–4.

[15] Broadcom Inc. *FBAR Filters*. Accessed: Jun. 12, 2020. [Online]. Available: https://www.broadcom.com/products/wireless/fbar/filters/

[16] Qorvo. *RF Filters*. Accessed: Jun. 12, 2020. [Online]. Available: http://www.qorvo.com/

[17] F. Martin, P. Muralt, M.-A. Dubois, and A. Pezous, "Thickness dependence of the properties of highly C-axis textured AlN thin films," *J. Vac. Sci. Technol. A*, vol. 22, no. 2, pp. 361–365, Feb. 2004.

[18] K. M. Howell, W. Bashir, A. De Pastina1, R. Matloub, P. Muralt, and L. G. Villanueva, "Effect of AlN seed layer on crystallographic characterization of piezoelectric AlN," *J. Vac. Sci. Technol. A, Vac. Surf. Films*, vol. 37, no. 2, 2019, Art. no. 021504.

[19] Akoustis Tech. *Filters*. Accessed: Jun. 12, 2020. [Online]. Available: https://akoustis.com/products/filters/

[20] S. Leone *et al.*, "Metal-organic chemical vapor deposition of aluminum scandium nitride," *Phys. Status Solidi-Rapid Res. Lett.*, vol. 14, no. 1, Nov. 2019, Art. no. 1900535.

Authorized licensed use limited to: Georgia Institute of Technology. Downloaded on July 09,2020 at 05:52:30 UTC from IEEE Xplore. Restrictions apply.

This article has been accepted for inclusion in a future issue of this journal. Content is final as presented, with the exception of pagination.

[21] M. T. Hardy, B. P. Downey, D. J. Meyer, N. Nepal, D. F. Storm, and D. S. Katzer, "Epitaxial ScAlN etch-stop layers grown by molecular beam epitaxy for selective etching of AlN and GaN," *IEEE Trans. Semicond. Manuf.*, vol. 30, no. 4, pp. 475–479, Oct. 2017.

[22] Z. Hao *et al.*, "Single crystalline ScAlN surface acoustic wave resonators with large figure of merit ($Q \times k_t{}^2$)," in *IEEE MTT-S Int. Microw. Symp. Dig.*, Boston, MA, USA, Jun. 2019, pp. 786–789.

[23] M. Park *et al.*, "A 10 GHz single crystalline Sc-AlN lamb-wave resonator," in *Proc. IEEE Transducers Conf.*, Berlin, Germany, Jun. 2019, pp. 450–453.

[24] A. Ansari, "Single crystalline scandium aluminum nitride: An emerging material for 5G acoustic filters," in *IEEE MTT-S Int. Microw. Symp. Dig.*, Boston, MA, USA, May 2019, pp. 1–3.

[25] M. Park, J. Wang, R. Dargis, A. Clark, and A. Ansari, "Super high-frequency scandium aluminum nitride crystalline film bulk acoustic resonators," in *Proc. IEEE Int. Ultrason. Symp.*, Glasgow, Scottland, Oct. 2019, pp. 1689–1692.

[26] M. B. Panish, "Molecular beam epitaxy," *Science*, vol. 208, no. 4446, pp. 916–922, 1980.

[27] R. Dargis *et al.*, "Single-crystal multilayer nitride, metal, and oxide structures on engineered silicon for new-generation radio frequency filter applications," *Phys. Status Solidi Appl. Mater. Sci.*, vol. 217, no. 7, pp. 1–8, Jan. 2020.

[28] P. M. Mayrhofer, C. Eisenmenger-Sittnner, M. Stöger-Pollach, H. Euchner, A. Bittner, and U. Schmid, "The impact of argon admixture on the C-axis oriented growth of direct current magnetron sputtered $Sc_xAl_{1-x}N$ thin films," *J. Appl. Phys.*, vol. 115, no. 19, 2014, Art. no. 193505.

[29] M. D. Henry, R. Timon, T. R. Young, C. Nordquist, and B. Griffin, "AlN and ScAlN contour mode resonators for RF filters," *ECS Trans.*, vol. 77, no. 6, pp. 23–32, May 2017.

[30] A. Iqbal and F. Mohd-Yasin, "Reactive sputtering of aluminum nitride (002) thin films for piezoelectric applications: A review," *Sensors*, vol. 18, no. 6, pp. 1–21, Jun. 2018.

[31] H. C. L. Tsui *et al.*, "The effect of metal-rich growth conditions on the microstructure of $Sc_xGa_{1-x}N$ films grown using molecular beam epitaxy," *Phys. Status Solidi Appl. Mater. Sci.*, vol. 212, no. 12, pp. 2837–2842, 2015.

[32] S. Mertin *et al.*, "Piezoelectric and structural properties of C-axis textured aluminium scandium nitride thin films up to high scandium content," *Surf. Coatings Technol.*, vol. 343, pp. 2–6, Jun. 2018.

[33] M. A. Caro *et al.*, "Erratum: Piezoelectric coefficients and spontaneous polarization of ScAlN," *J. Phys. Condens. Matter*, vol. 27, no. 27, Jun. 2015, Art. no. 245901.

[34] T. Yanagitani and M. Suzuki, "Electromechanical coupling and gigahertz elastic properties of ScAlN films near phase boundary," *Appl. Phys. Lett.*, vol. 105, no. 12, pp. 1–5, 2014.

[35] N. Kurz *et al.*, "Experimental determination of the electro-acoustic properties of thin film AlScN using surface acoustic wave resonators," *J. Appl. Phys.*, vol. 126, no. 7, Aug. 2019, Art. no. 075106.

[36] G. Wingqvist, F. Tasnadi, A. Zukauskaite, J. Birch, H. Arwin, and L. Hultman, "Increased electromechanical coupling in W-$Sc_xAl_{1-x}N$," *Appl. Phys. Lett.*, vol. 97, no. 11, pp. 1–5, Aug. 2010.

[37] W. B. Wang *et al.*, "AlScN thin film based surface acoustic wave devices with enhanced microfluidic performance," *J. Micromech. Microeng.*, vol. 26, no. 7, Jun. 2016, Art. no. 075006.

[38] W. Wang *et al.*, "High performance AlScN thin film based surface acoustic wave devices with large electromechanical coupling coefficient," *Appl. Phys. Lett.*, vol. 105, no. 13, Sep. 2014, Art. no. 133502.

[39] J. T. Luo *et al.*, "Cost-effective and high frequency surface acoustic wave filters on ZnO: Fe/Si for low-loss and wideband application," *Appl. Phys. Lett.*, vol. 101, no. 17, pp. 10–13, Oct. 2012.

[40] C. Campbell, *Surface Acoustic Wave Devices and Their Signal Processing Applications*. New York, NY, USA: Academic, 1989.

[41] A. Lozzi, E. T.-T. Yen, P. Muralt, and L. G. Villanueva, "$Al_{0.83}Sc_{0.17}N$ contour-mode resonators with electromechanical coupling in excess of 4.5%," *IEEE Trans. Ultrason., Ferroelectr., Freq. Control*, vol. 66, no. 1, pp. 146–153, Jan. 2019.

[42] J. Zou, C.-M. Lin, A. Gao, and A. P. Pisano, "The multi-mode resonance in AlN Lamb wave resonators," *J. Microelectromech. Syst.*, vol. 27, no. 6, pp. 973–984, Dec. 2018.

[43] M. D. Henry, T. R. Young, and B. Griffin, "ScAlN etch mask for highly selective silicon etching," *J. Vac. Sci. Technol. B, Nanotechnol. Microelectron. Mater. Proces. Meas. Phenom.*, vol. 35, no. 5, Sep. 2017, Art. no. 052001.

[44] M. Ghatge, V. Felmetsger, and R. Tabrizian, "High $k_t{}^2 \cdot Q$ waveguide-based ScAlN-on-Si UHF and SHF resonators," in *Proc. IEEE Int. Freq. Contr. Symp.*, Olympic Valley, CA, USA, May 2018, pp. 5–8.

[45] I. Cimalla, C. Foerster, V. Cimalla, V. Lebedev, D. Cengher, and O. Ambacher, "Wet chemical etching of AlN in KOH solution," *Phys. Status Solidi C*, vol. 3, no. 6, pp. 1767–1770, Jun. 2006.

[46] J. R. Mileham, S. J. Pearton, C. R. Abernathy, J. D. MacKenzie, R. J. Shul, and S. P. Kilcoyne, "Wet chemical etching of AlN," *Appl. Phys. Lett.*, vol. 67, p. 1119, Jun. 1995.

[47] A. Gao, J. Zou, and S. Gong, "A 3.5 GHz AlN S1 Lamb mode resonator," in *Proc. IEEE Int. Ultrason. Symp.*, Washington, DC, USA, Sep. 2017, pp. 1–4.

[48] J. Zou, J. Liu, and G. Tang, "Transverse spurious mode compensation for AlN Lamb wave resonators," *IEEE Access*, vol. 7, pp. 67059–67067, 2019.

[49] M. Rinaldi, C. Zuniga, and G. Piazza, "5-10 GHz ALN contour-mode nanoelectromechanical resonators," in *Proc. IEEE Int. Conf. Micro Electro Mech. Syst.*, Sorrento, Italy, Jun. 2009, pp. 916–919.

[50] D. A. Feld, R. Parker, R. Ruby, P. Bradley, and S. Dong, "After 60 years: A new formula for computing quality factor is warranted," in *Proc. IEEE Ultrason. Symp.*, Beijing, China, Nov. 2008, pp. 431–436.

[51] V. J. Gokhale *et al.*, "Epitaxial bulk acoustic wave resonators as highly coherent multi-phonon sources for quantum acoustodynamics," *Nature Commun.*, vol. 11, no. 2314, pp. 1–9, May 2020.

[52] H. Zhu and J. E. Y. Lee, "AlN piezoelectric on silicon MEMS resonator with boosted Q using planar patterned phononic crystals on anchors," in *Proc. IEEE Int. Conf. Micro Electro Mech. Syst.*, Estoril, Portugal, Jan. 2015, pp. 797–800.

[53] Y. Lu *et al.*, "Elastic modulus and coefficient of thermal expansion of piezoelectric $Al_{1-x}Sc_xN$ (up to x = 0.41) thin films," *APL Mater.*, vol. 6, no. 7, Jul. 2018, Art. no. 076105.

[54] A. Mujahid and F. L. Dickert, "Surface acousticwave (SAW) for chemical sensing applications of recognition layers," *Sensors*, vol. 17, no. 12, pp. 1–26, Nov. 2017.

[55] W. Wang *et al.*, "Comparative study on microfluidic performance of ZnO surface acoustic wave devices on various substrates," *J. Electrochem. Soc.*, vol. 161, no. 10, pp. B230–B236, Jul. 2014.

Mingyo Park (Senior Member, IEEE) received the B.S. and M.S. degree in electrical and electronic engineering from Yonsei University, Seoul, South Korea, in 2014 and 2016, respectively. She is currently a pursuing the Ph.D. degree with the Department of Electrical and Computer Engineering, Georgia Institute of Technology, Atlanta, GA, USA.

Her research interests include phononic frequency combs and RF MEMS resonators and filters for super high-frequency (SHF) range applications. She was a recipient of the LG Display Education Scholarship in 2016.

Zhijian Hao (Senior Member, IEEE) received the B.S. degree in electrical engineering from the University of Michigan, Ann Arbor, MI, USA, in 2019. He is currently pursuing the Ph.D. degree with the Georgia Institute of Technology, Atlanta, GA, USA.

His research focuses include micro swarm robotics, MEMS sensors and actuators, and acoustic wave resonators. He was a recipient of the Otto and Jenny Krauss Fellowship at the Georgia Institute of Technology.

Rytis Dargis received the Electrical Engineering degree in physical electronics, the M.S. degree in applied physics, and the Ph.D. degree in materials science from the Kaunas University of Technology, Lithuania. He is currently a Principal Materials Research and Development Engineer, IQE Plc., NC, USA. His professional interest focuses on the development of epitaxial technology for new generation photonic and electronic devices. In this field, he authored many technological inventions and scientific publications. Before his career in industry, he spent a decade performing research at several European and USA academic institutions.

Authorized licensed use limited to: Georgia Institute of Technology. Downloaded on July 09,2020 at 05:52:30 UTC from IEEE Xplore. Restrictions apply.

This article has been accepted for inclusion in a future issue of this journal. Content is final as presented, with the exception of pagination.

Andrew Clark received the Ph.D. degree in electronic materials from the Australian National University in 1996. He is currently a Senior Director with New Technologies, IQE Plc, NC, USA, with responsibility for the rare earth materials program focused on nitride-based RF applications. He was previously VP Engineering at Translucent Inc., where he managed the development of rare earth oxide technology. He has a 30-year career ranging from startups to high-volume manufacturing of compound materials, serving the photonics and electronics industries, and utilizing MOCVD and MBE platforms.

Azadeh Ansari (Member, IEEE) received the B.S. degree in electrical engineering from the Sharif University of Technology, Tehran, Iran, in 2010, and the M.S. and Ph.D. degrees in electrical engineering from the University of Michigan, Ann Arbor, in 2013 and 2016, respectively, focusing upon III–V semiconductor and MEMS devices and microsystems for RF applications. She is currently an Assistant Professor with the School of Electrical and Computer Engineering, Georgia Institute of Technology. Prior to joining the ECE Faculty with the Georgia Tech, she was a Post-Doctoral Scholar with the Department of Physics, California Institute of Technology, from September 2016 to July 2017. Her research interests lie in the area of nano/micro electromechanical systems (N/MEMS) and radio frequency (RF) integrated systems. She was a recipient of the 2017 ProQuest Distinguished Dissertation Award from the University of Michigan for her research on GaN Integrated Microsystems for RF Applications. She received the University of Michigan Richard and Eleanor Towner Prize for outstanding Ph.D. research in 2016.

Authorized licensed use limited to: Georgia Institute of Technology. Downloaded on July 09,2020 at 05:52:30 UTC from IEEE Xplore. Restrictions apply.